
PARTICLE-IN-CELL SIMULATIONS OF SUNWARD AND ANTI-SUNWARD WHISTLER WAVES IN THE SOLAR WIND

A PREPRINT

Ilya V. Kuzichev¹, Ivan Y. Vasko^{2,3}, Anton V. Artemyev^{4,3}, Stuart D. Bale², Forrest S. Mozer²
¹ilya.kuzichev@njit.edu

¹New Jersey Institute of Technology, CSTR, 323 MLK Blvd, Newark, NJ 07102-1982, USA

²Space Sciences Laboratory, University of California, Berkeley, CA 94720-7450, USA

³Space Research Institute of RAS, 84/32 Profsoyuznaya Str, Moscow 117997, Russia

⁴Institute of Geophysics and Planetary Physics, University of California, Los Angeles, CA 90065-1567, USA

April 3, 2023

ABSTRACT

Spacecraft observations showed that electron heat conduction in the solar wind is probably regulated by whistler waves, whose origin and efficiency in electron heat flux suppression is actively investigated. In this paper, we present Particle-In-Cell simulations of a combined whistler heat flux and temperature anisotropy instability that can operate in the solar wind. The simulations are performed in a uniform plasma and initialized with core and halo electron populations typical of the solar wind. We demonstrate that the instability produces whistler waves propagating both along (anti-sunward) and opposite (sunward) to the electron heat flux. The saturated amplitudes of both sunward and anti-sunward whistler waves are strongly correlated with their *initial* linear growth rates, $B_w/B_0 \sim (\gamma/\omega_{ce})^\nu$, where for typical electron betas we have $0.6 \lesssim \nu \lesssim 0.9$. The correlations of whistler wave amplitudes and spectral widths with plasma parameters (electron beta and temperature anisotropy) revealed in the simulations are consistent with those observed in the solar wind. The efficiency of electron heat flux suppression is positively correlated with the saturated amplitude of sunward whistler waves. The electron heat flux can be suppressed by 10–60% provided that the saturated amplitude of sunward whistler waves exceeds about 1% of background magnetic field. Other experimental applications of the presented results are discussed.

1 Introduction

The early spacecraft measurements at 0.3–5 au [1, 2, 3] and recent Parker Solar Probe (PSP) measurements at 0.1–0.3 au [4] showed that electron heat conduction in the solar wind cannot be described by the Spitzer-Härm law [5]. The reason is that solar wind electrons are only weakly-collisional; the collisional mean free path typically exceeds the inverse gradient scale length of electron temperature in the heliosphere [6, 7, 4]. In accordance with previous observations at 1 au [8, 9, 10], PSP and Helios measurements showed that electron heat flux is bounded by a threshold dependent on local electron beta [11, 4, 12]. The beta-dependent threshold indicates that wave-particle interactions are probably regulating electron heat conduction in the solar wind, and whistler waves were suggested to be the most likely wave activity involved in the regulation process [13, 14, 3]. The modern spacecraft measurements have substantially advanced the understanding of electron heat conduction in the solar wind, but still have not established the heat flux regulation mechanism.

Whistler waves involved in the electron heat flux regulation can be of different origin. First, the electron heat flux can be regulated by whistler waves naturally produced by turbulence cascade [15, 16, 17, 18]. While early observations of broadband magnetic field fluctuations between ion and electron kinetic scales were indeed interpreted in terms of whistler waves [19, 20], the modern spacecraft measurements showed that magnetic field turbulence at these scales is dominated by kinetic Alfvén waves [21]. The presence of broadband whistler mode fluctuations cannot be entirely ruled out though [22] and the contribution of magnetic field turbulence to the electron heat flux regulation remains to

be quantified [17]. On the other hand, whistler waves involved in the heat flux regulation can be produced by various electron-driven instabilities [e.g., 23, 14, 24].

The velocity distribution function of electrons in a pristine solar wind consists of a dense thermal core population contributing about 90% of total electron density and tenuous superthermal halo and strahl populations carrying the most of the electron heat flux [e.g., 25, 26, 27, 28]. The core and halo populations are relatively isotropic and can be described in the plasma rest frame by sunward-drifting Maxwell and anti-sunward drifting κ -distributions, respectively. In contrast, the strahl is a highly anisotropic population collimated around local magnetic field and streaming anti-sunward. It was recently suggested that oblique whistler waves driven by the strahl can potentially regulate the electron heat flux [29, 30]. Numerical simulations showed this instability can indeed suppress the electron heat flux by pitch-angle scattering the strahl and converting it into more or less isotropic halo [31, 32, 33]. The instability of oblique whistler waves could, in principle, explain the observed radial evolution of halo and strahl densities [25, 26] as well as the observed beta-dependent threshold on the electron heat flux [4, 12]. However, there are currently several indications that this instability *does not* substantially regulate electron heat conduction in the solar wind.

First, PSP and Helios measurements at 0.1–1 au showed the strahl parameters are statistically well below the instability threshold [34]. Second, PSP measurements at 0.1–0.5 au revealed the radial evolution of halo and strahl densities to be inconsistent with the halo being produced via pitch-angle scattering of the strahl [35]. Consistent with that, the recent analysis showed that halo electrons propagating sunward (almost a half of the halo population) originate in the outer heliosphere rather than evolve from the strahl [36]. Third, whistler waves observed in a pristine solar wind at 0.1–1 au usually propagate within a few tens of degrees of local magnetic field [37, 38, 39, 10, 40, 41, 12]. Oblique whistler waves do present in the solar wind, but typically occur around stream interaction regions and coronal mass ejections [42, 43]; thus, they are not likely substantially involved in the regulation of electron heat conduction in the solar wind.

The fact that whistler waves in the solar wind are typically quasi-parallel stimulates the analysis of their origin and effects. The early theoretical analysis by [23, 44] showed that whistler waves in the solar wind can be produced by the whistler heat flux instability (WHFI). This instability operates, when core and halo populations, isotropic or parallel-anisotropic in temperature, drift relative to each other parallel to local magnetic field; there is a heat flux parallel to the halo drift (but the net current in the plasma frame is zero) and the fastest-growing whistler waves propagate parallel to the heat flux. A strahl population that is drifting anti-sunward does not affect the WHFI, because the unstable whistler waves are resonant only with a fraction of sunward-propagating halo electrons. The recent observations showed that the WHFI indeed operates in the solar wind and produces whistler waves propagating anti-sunward [45]. The recent Particle-In-Cell simulations showed that the WHFI can produce whistler waves with properties consistent with solar wind observations, but *cannot* regulate the electron heat flux [46], contrary to previous speculations [14, 8, 47].

The fraction of whistler waves produced in the solar wind via the WHFI is still not known [10, 11]. There are indications that whistler waves can be also produced by the instability associated with a perpendicular temperature anisotropy of the halo population [48, 11]. These indications consist in statistically significant observations of the halo population with perpendicular temperature anisotropy [49, 11, 50, 51, 28] and preferential occurrence of whistler waves in association with isotropic or perpendicular anisotropic halo [45, 10, 11]. The recent reports of sunward and anti-sunward propagating whistler waves in near-Sun solar wind are also of relevance [52, 53].

In this paper, we present Particle-In-Cell simulations of a combined whistler heat flux and temperature anisotropy instability that is potentially operating in the solar wind and capable of producing both sunward and anti-sunward whistler waves. We determine saturation amplitudes of the whistler waves along with their dependence on plasma parameters and demonstrate that these amplitudes can be estimated using *initial* linear growth rates of the whistler waves. The efficiency of this instability in electron heat flux regulation and other experimental applications of the presented results are discussed.

2 Linear instability and simulation setup

We use Particle-in-Cell TRISTAN-MP code [54] and perform 1D3V simulations restricted to whistler waves propagating parallel and anti-parallel to background magnetic field. Ions are assumed to be an immobile neutralizing background. Electrons are represented by core and halo populations, whose initial velocity distribution functions (VDF) in the plasma frame in a non-relativistic limit, which is the case in our simulations, are described by Maxwell distributions

$$f_{\alpha}(\mathbf{v}) = \mathcal{N}_{\alpha} \exp \left[-\frac{m_e(v_{\parallel} - u_{\alpha})^2}{2 T_{\alpha}} - \frac{m_e v_{\perp}^2}{2 A_{\alpha} T_{\alpha}} \right], \quad (1)$$

where $\alpha = c, h$ correspond to core and halo populations, v_{\parallel} and v_{\perp} are velocities parallel and perpendicular to background magnetic field, $\mathcal{N}_{\alpha} = n_{\alpha} A_{\alpha}^{-1} (m_e / 2\pi T_{\alpha})^{3/2}$ is the normalization constant, n_{α} , u_{α} , T_{α} and A_{α} are respectively

Table 1: The electron parameters for simulation sets I–III: each set consist of 25 simulation runs performed at a fixed value of core electron beta β_c and 25 pairs of core drift velocity u_c/v_A and halo temperature anisotropy A_h ; the values of A_h are from 1.1. to 1.5 with a step of 0.1, while the values of u_c/v_A are from -1.5 to -7.5 with a step of 1.5. In all simulation runs the relative core electron density was $n_c/n_0 = 0.85$, the ratio of halo and core parallel temperatures was $T_h/T_c = 6$, and the core electron population was isotropic, $A_c = 1$.

run sets	β_c	$-u_c/v_A$	A_h
I	0.3	1.5:1.5:7.5	1.1:0.1:1.5,
II	1	1.5:1.5:7.5	1.1:0.1:1.5,
III	3	1.5:1.5:7.5	1.1:0.1:1.5,

densities, drift velocities, parallel temperatures and temperature anisotropies. The electron current is assumed to be zero, $n_c u_c + n_h u_h = 0$. The electron heat flux is parallel to background magnetic field and carried predominantly by the halo population, $q_e \approx -n_c u_c T_h (3/2 + A_h)$, because the halo is several times hotter than the core population, $T_h/T_c \approx 3-7$ [e.g., 25, 28].

The combination of core and halo populations relatively well describes the electron VDF beyond 0.2 au, where the halo density is several times larger than the strahl density [25, 28, 35]. Although the halo population is better described by a κ -distribution [e.g., 25], we consider Maxwellian halo to reduce the number of free parameters. The use of a κ -distribution would not affect the critical results of this study. The linear analysis of a combined whistler heat flux and temperature anisotropy instability shows that the growth rate normalized to electron cyclotron frequency ω_{ce} depends on the wavenumber normalized to electron inertial length c/ω_{pe} and the following parameters [48]

- $\beta_c = 8\pi n_c T_c / B_0^2$: core electron beta.
- n_c/n_0 : core density relative to total electron density, $n_0 = n_c + n_h$.
- u_c/v_A : core drift velocity in units of Alfvén speed, $v_A = B_0(4\pi n_0 m_p)^{-1/2}$.
- T_h/T_c : ratio of halo and core parallel temperatures.
- A_c and A_h : core and halo temperature anisotropies.

Note that linear stability as well as nonlinear evolution also depend on the ratio between electron plasma and cyclotron frequencies, but this dependence is negligible once $\omega_{pe}/\omega_{ce} \gg 1$ [46, 48]. In this paper, we keep $n_c/n_0 = 0.85$, $T_h/T_c = 6$, $A_c = 1$, and present numerical simulations at various combinations of β_c , u_c/v_A and A_h . The typical values of these parameters in the solar wind are $\beta_c = 0.1-10$, $|u_c|/v_A = 1-7$ and $A_h = 1.1-1.5$ [49, 9, 50, 51, 11, 28]. The values of these parameters used in three sets of simulations (25 runs per set) are presented in Table 1.

We performed the simulations at $\omega_{pe}/\omega_{ce} \sim 10$ that is about ten times smaller than in the realistic solar wind. More precisely, in all simulations, we assumed core electron temperature T_c of 2 keV, and computed ω_{pe}/ω_{ce} using the following identity, $\omega_{pe}/\omega_{ce} \equiv (\beta_c n_0/n_c)^{1/2} (m_e c^2/2T_c)^{1/2}$; for $\beta_c = 0.3-3$ we have $\omega_{pe}/\omega_{ce} \approx 7-20$. In all simulation runs, the length of the simulation box was $L \approx 105 c/\omega_{ce}$ or, for $\beta_c = 1$, about $1300 c/\omega_{pe}$. The temporal and spatial integration steps were $0.09 \omega_{pe}^{-1}$ and $0.2 c/\omega_{pe}$, both adequate to resolve the expected whistler waves. The number of particles per cell for each population was $4 \cdot 10^4$. We will preface the presentation of simulation results by linear stability analysis.

Figure 1 presents results of linear stability analysis of whistler waves at fixed values of core electron beta and halo temperature anisotropy ($\beta_c = 1$ and $A_h = 1.3$), but various values of electron heat flux determined by core drift velocity u_c/v_A . Panels (a) and (b) present the dispersion curves and growth rates of whistler waves propagating parallel and anti-parallel to the electron heat flux. When the electron heat flux is absent ($u_c/v_A = 0$), identical parallel and anti-parallel whistler waves are unstable due to the halo temperature anisotropy. The presence of electron heat flux breaks the symmetry resulting in larger growth rates of whistler waves propagating parallel to the electron heat flux. Panels (c)–(e) present the maximum growth rates along with corresponding frequencies and wave numbers of parallel and anti-parallel whistler waves unstable at various values of u_c/v_A . In the considered range of u_c/v_A values, the parameters of the fastest-growing parallel whistler waves barely vary ($\gamma_+/\omega_{ce} \approx 0.01$, $\omega_+/\omega_{ce} \approx 0.1$ and $k_+c/\omega_{pe} \approx 0.34$). In contrast, the maximum growth rate of anti-parallel whistler waves monotonously decreases from $\gamma_-/\omega_{ce} \approx 0.01$ to 10^{-3} ; the frequency and wave number monotonously decrease by a factor of a few.

3 Results of simulations at $\beta_c = 1$ and $A_h = 1.3$

Figure 2 presents results of a simulation run performed at $\beta_c = 1$, $A_h = 1.3$ and $u_c/v_A = -3$. We consider the dynamics of magnetic field $\delta\mathbf{B}(x,t) = \delta B_y(x,t)\hat{y} + \delta B_z(x,t)\hat{z}$ perpendicular to background magnetic field $B_0\hat{x}$. Panel (a) presents the magnetic field magnitude $\delta B(x,t)/B_0$ and demonstrates the growth of magnetic field fluctuations propagating both parallel and anti-parallel to the electron heat flux. Using Fourier transform, $\delta\mathbf{B}(x,t) = \int \delta\mathbf{B}_{k\omega} e^{i(kx-\omega t)} dk d\omega$, we decompose magnetic field fluctuations into those propagating parallel and anti-parallel to the electron heat flux, $\delta\mathbf{B}(x,t) = \delta\mathbf{B}_+(x,t) + \delta\mathbf{B}_-(x,t)$, where $\delta\mathbf{B}_+(x,t) = \int_{\omega/k>0} \delta\mathbf{B}_{k\omega} e^{i(kx-\omega t)} dk d\omega$ and $\delta\mathbf{B}_-(x,t) = \int_{\omega/k<0} \delta\mathbf{B}_{k\omega} e^{i(kx-\omega t)} dk d\omega$. Both $\delta\mathbf{B}_+$ and $\delta\mathbf{B}_-$ have right-hand polarization (not shown here) and correspond to parallel and anti-parallel whistler waves expected based on linear stability analysis (Figure 1). Panels (b) and (c) show that over the computation time parallel and anti-parallel whistler waves reach peak amplitudes of about $0.1B_0$ and $0.05B_0$, respectively.

Figure 3 presents averaged amplitudes and growth rates of the parallel and anti-parallel whistler waves. Panel (a) shows the temporal evolution of magnetic field amplitudes averaged over the simulation box, $\langle \delta B_{\pm} \rangle = \left[L^{-1} \int_0^L |\delta\mathbf{B}_{\pm}|^2 dx \right]^{1/2}$, and shows that within the computation time parallel and anti-parallel whistler waves saturate and the saturated amplitudes are $B_w^+/B_0 \approx 0.04$ and $B_w^-/B_0 \approx 0.02$. Panel (b) presents the temporal evolution of whistler wave growth rates computed as $d/dt [\ln \langle \delta B_{\pm} \rangle]$. The initial growth rates of parallel and anti-parallel whistler waves are respectively around 0.01 and 0.003 ω_{ce} , both consistent within a few tens of percent with linear stability results (Figure 1c).

Figure 4 presents results of simulation runs performed at $\beta_c = 1$, $A_h = 1.3$ and various values of u_c/v_A indicated in panels (c)–(e) in Figure 1. In all these simulation runs, parallel and anti-parallel whistler waves saturated within the computation time and we computed the averaged amplitudes B_w^+ and B_w^- reached by the end of each simulation run. Panel (a) shows that the saturated amplitude B_w^+ of parallel whistler waves is around $0.04B_0$ and varies by less than several tens of percent over the considered range of u_c/v_A values. In contrast, the saturated amplitude B_w^- of anti-parallel whistler waves monotonously decreases from 0.025 to $0.005B_0$. Interestingly, according to panel (a) the dependencies of the saturated amplitudes B_w^+ and B_w^- on u_c/v_A are almost identical with those of *initial* linear growth rates γ_+ and γ_- . Panel (b) demonstrates that the ratio B_w^+/B_w^- is closely correlated with γ_+/γ_- and the best power law fit is $B_w^+/B_w^- \approx (\gamma_+/\gamma_-)^{0.73}$. This relation naturally predicts lower saturation amplitudes of anti-parallel whistler waves compared to parallel whistler waves, because the former always have lower *initial* linear growth rates in our model (Figure 1).

Figure 5 presents the temporal evolution of the electron heat flux in the considered simulation runs. We demonstrate the electron heat flux variation $\delta q_e(t) = [q_e(t) - q_e(0)]/q_e(0)$ in percents, where $q_e(t)$ is the electron heat flux averaged over the simulation box and $q_e(0)$ is its initial value. The electron heat flux suppression is most efficient, $\delta q_e \approx -10\%$, in the simulation run with $u_c/v_A = -1.5$, while the efficiency drops to about 1% at $u_c/v_A = -7.5$. There will be a natural positive correlation between the efficiency of electron heat flux suppression and the amplitude of anti-parallel whistler waves (shown further), because B_w^-/B_0 is larger for smaller values of core electron drift velocity $|u_c|/v_A$ (Figure 4a). Note that electron heat flux suppression of 10% is relatively large compared to a few percent variation observed in the simulations of a pure whistler heat flux instability [46].

4 Results of all simulations

Figure 6 presents averaged amplitudes B_w^+ and B_w^- of parallel and anti-parallel whistler waves for all the 75 simulation runs (Table 1). Note that we demonstrate a whistler wave amplitude only if the initial linear growth rate of the whistler wave is larger than $10^{-3} \omega_{ce}$; otherwise the computation time of $5000 \omega_{ce}^{-1}$ is insufficient for whistler waves to saturate. For this reason the number of points corresponding to parallel and anti-parallel whistler waves in panels (a)–(c) can be different and also less than 25. Panels (a)–(c) show that at a fixed core electron beta β_c the saturated amplitudes are larger for larger halo temperature anisotropy A_h and increase by a factor of a few between $A_h = 1.1$ and 1.5. Also both parallel and anti-parallel whistler waves tend to saturate at larger amplitudes for larger core electron betas; for identical anisotropies saturated amplitudes increase by a factor of a few between $\beta_c = 0.3$ and 3. The observed dependencies of the saturated amplitudes on the halo temperature anisotropy and other plasma parameters could be actually inferred from a more fundamental relation to be presented below.

Figure 7 shows that at every fixed core electron beta the saturated amplitudes of parallel and anti-parallel whistler waves are well-correlated with their *initial* linear growth rates. The observed trends can be fitted to power-law func-

Table 2: The best-fit parameters of the power-law fit given by Eq. (2) between the saturated amplitudes of sunward and anti-sunward whistler waves and their initial linear growth rates. The best power-law fits are demonstrated in Figure 7.

β_c	C_+	v_+	C_-	v_-
0.3	0.44	0.66	1.76	0.91
1	1.2	0.82	0.53	0.66
3	1.84	0.9	0.39	0.58

tions

$$B_w^\pm/B_0 = C_\pm(\gamma_\pm/\omega_{ce})^{v_\pm}, \quad (2)$$

where the best fit parameters C_\pm and v_\pm are indicated in the panels and presented in Table 2. The power-law indexes and multipliers corresponding to parallel and anti-parallel whistler waves are different and vary with core electron beta; in the considered range of core electron beta, the power law indexes vary in a relatively narrow range, $0.6 \lesssim v_\pm \lesssim 0.9$. The fundamental relation between the saturated amplitude and the initial linear growth rate naturally predicts larger amplitudes of parallel and anti-parallel whistler waves for larger anisotropies and core electron betas, because the increase of these parameters results in larger linear growth rates [48]. This relation also indicates that anti-parallel whistler waves are expected to saturate at lower amplitudes than parallel whistler waves, because the presence of electron heat flux results in smaller growth rates of the former (Figure 1). Note that Eq. (2) naturally explains the correlations reported in the previous section in Figure 4.

Figure 8 demonstrates the efficiency of electron heat flux suppression quantified by the relative heat flux variation δq_e reached at the saturation stage. We present δq_e only if both parallel and anti-parallel whistler waves saturated within the computation time. Panel (a) shows that electron heat flux suppression is within about 10% at low temperature anisotropies ($A_h \lesssim 1.1$), but can be as large as 60% at $A_h = 1.5$. At a fixed halo temperature anisotropy, the electron heat flux suppression is more efficient at larger core electron betas. The efficiency of electron heat flux suppression is expected to correlate with the saturated whistler wave amplitudes, since the latter are positively correlated with both electron beta and temperature anisotropy (Figure 5). Panel (b) shows that electron heat flux suppression δq_e is positively correlated with the saturated amplitude of anti-parallel whistler waves. The heat flux suppression is within 10% at $B_w^-/B_0 \lesssim 0.01$, but can be as large as 10–60% at $B_w^-/B_0 \gtrsim 0.01$. The electron heat flux suppression δq_e is also correlated with B_w^+/B_0 (not shown here), but this correlation does not have direct experimental applications (see Section 5).

We address spectral properties of the whistler waves by computing power spectral densities of parallel and anti-parallel whistler waves over the saturation stage, $\text{PSD}_\omega^\pm = \langle |\int \delta \mathbf{B}_\pm(x, t) e^{i\omega t} dt|^2 \rangle$, where the integration is over a time period where the instability has saturated, while $\langle \cdot \rangle$ stands for spatial averaging over the simulation box. Gaussian fitting was done to determine the central wave frequency and the spectral width of the power spectral densities PSD_ω^\pm . Figure 9a demonstrates that both parallel and anti-parallel whistler waves have comparable relative spectral widths, $\Delta\omega_\pm/\omega_\pm \sim 0.3\text{--}0.8$. It is noteworthy that the relative spectral widths tend to be larger for larger core electron betas and positively correlated with initial linear growth rate of the whistler waves. The frequency of the saturated whistler waves is consistent within a few tens of percent with the frequency of initially fastest-growing whistler waves (not shown here).

5 Discussion

We presented the first Particle-In-Cell simulations of a combined whistler heat flux and temperature anisotropy instability, which generalize our previous simulations of a pure whistler heat flux instability with isotropic halo population [46]. In contrast to the pure whistler heat flux instability capable of producing only whistler waves propagating parallel to the electron heat flux (anti-sunward), the combined whistler heat flux and temperature anisotropy instability produces both whistler waves propagating parallel (anti-sunward) and anti-parallel (sunward) to the electron heat flux. We showed that the saturated amplitudes of the whistler waves are correlated their initial linear growth rates, $B_w/B_0 \approx C(\gamma/\omega_{ce})^v$, where parameters C and v are a bit different for sunward and anti-sunward whistler waves. For typical solar wind conditions considered in our simulations the power-law index varies in a relatively narrow range, $0.6 \lesssim v \lesssim 0.9$ (Table 2). A similar scaling relation, though revealed using a few simulation runs, was reported for anti-sunward whistler waves produced by the pure whistler heat flux instability [46].

Whistler waves in our simulations saturated at $B_w/B_0 \sim 0.01$, because we required sufficiently high initial linear growth rates, $\gamma/\omega_{ce} \gtrsim 10^{-3}$, to save computational resources (Figure 7). Whistler waves with such high amplitudes

rarely occur in the solar wind; the observed amplitudes are typically around $10^{-3}B_0$ [10, 55, 41] and, hence, correspond to initial growth rates of about $10^{-4}\omega_{ce}$. Nevertheless, we believe the revealed scaling relation is valid in a wide range of growth rates and its predictions can be compared with solar wind observations. Since linear growth rates of both sunward and anti-sunward whistler waves are larger for larger electron beta and temperature anisotropy [48], we expect whistler wave amplitudes to be positively correlated with these parameters. The corresponding positive correlations were indeed observed in the solar wind [10]. We also showed that the whistler waves have relatively large spectral widths positively correlated with electron beta (Figure 9a). Spacecraft observations revealed similar values of the spectral width and its positive correlation with the electron beta [10].

The revealed scaling relation (2) *does not* correspond to whistler wave saturation via nonlinear trapping of cyclotron resonant electrons, which would occur once the bounce frequency of trapped electrons, $\omega_T \approx (kv_{\perp}eB_w/m_e c)^{1/2}$, is comparable to the initial linear growth rate γ , where $v_{\perp} \sim (2T_h/m_e)^{1/2}$ is a typical perpendicular speed of resonant electrons [56, 57, 58]. The saturation via nonlinear trapping would result in $B_w/B_0 \propto (\gamma/\omega_{ce})^2$ that is inconsistent with the observed scaling relation. The nonlinear trapping does not occur when whistler waves have a sufficiently large spectral width or low amplitude such that the resonant velocity $v_{\parallel} = (\omega - \omega_{ce})/k$ is distributed in a range much wider than the nonlinear resonance width ω_T/k [59, 57]. In this case the nonlinear evolution and saturation of whistler waves could be described within the quasi-linear theory. Thus, the quasi-linear description applies provided that

$$\frac{\partial}{\partial \omega} \left(\frac{\omega - \omega_{ce}}{k} \right) \Delta \omega \gg \frac{\omega_T}{k},$$

which can be rewritten as follows

$$\frac{\Delta \omega}{\omega} \gg \left(\frac{B_w}{B_0} \right)^{1/2} \left(\frac{\beta \omega}{\omega_{ce} - \omega} \right)^{1/4}, \quad (3)$$

where $\beta = \beta_h n_0/n_h$ and $\beta_h = 8\pi n_h T_h/B_0^2$ is the halo electron beta. We computed the ratio between the left- and right-hand sides of Eq. (3) for sunward and anti-sunward whistler waves observed in the simulations. Figure 9b shows that both sunward and anti-sunward whistler waves have relatively large spectral widths or low amplitudes to make quasi-linear description applicable at initial growth rates realistic of the solar wind. The same statement was shown to be valid for whistler waves actually observed in the solar wind [10]. Note that quasi-linear description may fail at growth rates exceeding $0.01\omega_{ce}$, which are not realistic of solar wind plasma according to typically observed amplitudes of $10^{-3}B_0$. The derivation of the scaling relation (2) using quasi-linear computations will be presented in a separate paper, where its validity in case of both Maxwell and κ -distributions of the halo population will be demonstrated.

The combined whistler heat flux and temperature anisotropy instability is likely operating in the solar wind. Among strong indications for its operation are statistically significant observations of the halo population with perpendicular temperature anisotropy [49, 11, 28] and preferential occurrence of whistler waves in association with isotropic or perpendicular anisotropic halo [45, 10, 11]. The operation of this instability may seem to be at conflict with recent reports of predominantly anti-sunward whistler waves in the solar wind [41]. In fact, the small and still uncertain occurrence of sunward whistler waves can be caused by several reasons. First, whistler waves in the solar wind are indeed produced by other instabilities including a whistler heat flux instability with isotropic or parallel-anisotropic halo electrons [45] and a somewhat similar instability associated with a deficit of sunward electrons [40]; both these instabilities produce only anti-sunward whistler waves. Second, even in the presence of a perpendicular halo temperature anisotropy, the electron heat flux breaks the symmetry between sunward and anti-sunward whistler waves resulting in smaller growth rates and, hence, smaller saturated amplitudes of the former; therefore, the presence of sunward whistler waves is more likely obscured in magnetic field spectra by solar wind turbulence.

Our previous simulations showed that anti-sunward whistler waves produced by the pure whistler heat flux instability are not efficient in the electron heat flux suppression [46]. In contrast, the combined whistler heat flux and temperature anisotropy instability can be more efficient in the electron heat flux suppression, especially at sufficiently large core electron beta and halo temperature anisotropy; at $\beta_c \gtrsim 3$ and $A_h \gtrsim 1.3$ the electron heat flux can be suppressed by up to 30–60% (Figure 8a). Note that more efficient suppression of the electron heat flux at higher electron betas is consistent with spacecraft observations [e.g., 8, 10, 4], while the effect of the halo anisotropy has not been addressed experimentally yet. Importantly, the efficiency of electron heat flux suppression is positively correlated with the amplitude B_w/B_0 of sunward whistler waves and the electron heat flux can be suppressed by more than 10–60% at $B_w/B_0 \gtrsim 0.01$ (Figure 9b). This correlation allows the observed amplitude of sunward whistler waves to serve as an indicator of the efficiency of electron heat flux suppression. Since whistler waves in the solar wind have typical amplitudes below a few percent of background magnetic field (a fraction of them is sunward), we expect the typical efficiency of electron heat flux suppression within about 10%. The recent reports of sunward whistler waves with amplitudes of $0.1B_0$ [52, 53] indicate however that electron heat flux can be occasionally suppressed by more than

60%. Note that the amplitude of anti-sunward whistler waves cannot similarly indicate the efficiency of electron heat flux suppression, since anti-sunward whistler waves are also produced by other instabilities proved to be inefficient in electron heat flux suppression [45, 46].

In conclusion, the combined whistler heat flux and temperature anisotropy instability is very likely operating in the solar wind and capable of producing both sunward and anti-sunward whistler waves. The presented Particle-In-Cell simulations revealed correlations between whistler wave properties (amplitude and spectral width) and various plasma parameters, which are consistent with previous solar wind observations. This instability can be efficient in electron heat flux suppression and the amplitude of sunward whistler waves can serve as an indicator of the efficiency. We expect future spacecraft measurements to reveal the occurrence and amplitude of sunward whistler waves and allow establishing the contribution of this instability to the electron heat flux suppression in the solar wind.

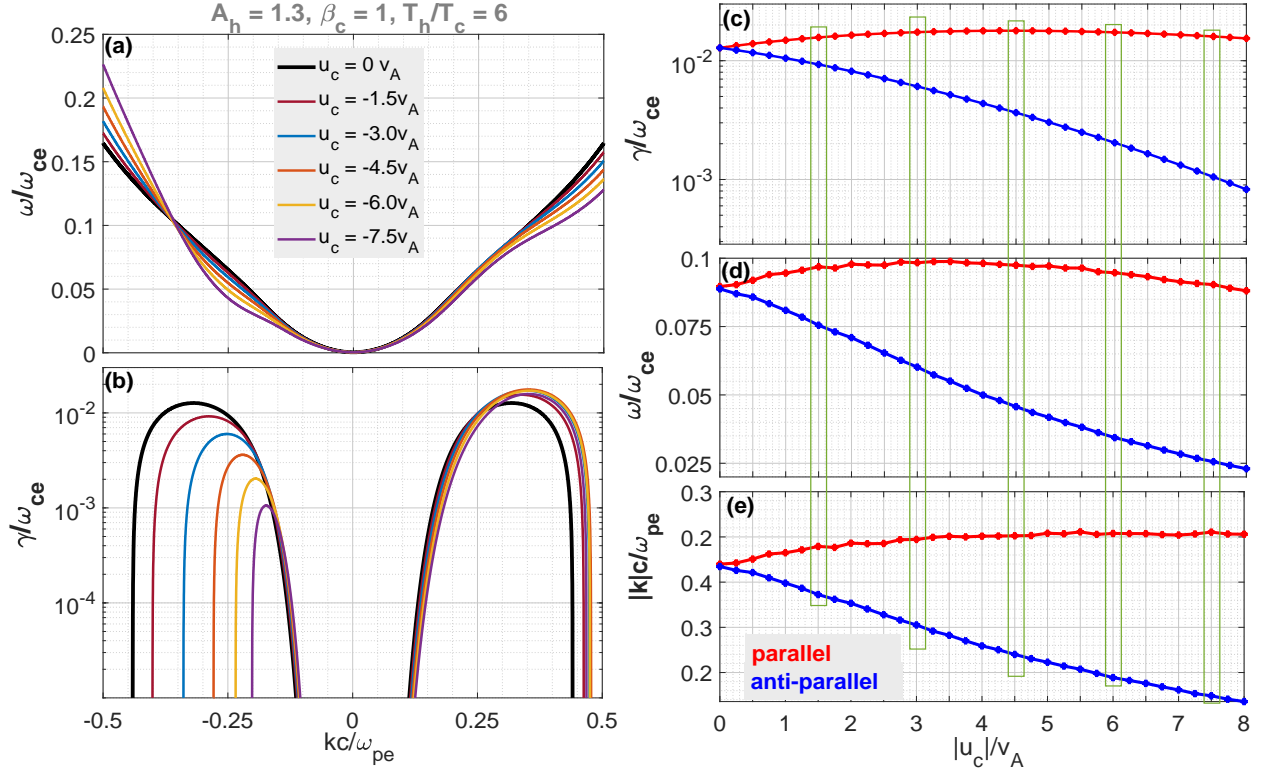


Figure 1: The results of linear stability analysis of a combined whistler heat flux and temperature anisotropy instability at fixed core electron beta and halo temperature anisotropy ($\beta_c = 1$ and $A_h = 1.3$), but various values of the electron heat flux set by core drift velocity u_c/v_A . Panels (a) and (b) present dispersion curves (ω/ω_{ce} vs. kc/ω_{pe}) and growth rates (γ/ω_{ce} vs. kc/ω_{pe}) of whistler waves propagating parallel ($k > 0$) and anti-parallel ($k < 0$) to the electron heat flux, where ω_{ce} and ω_{pe} are respectively electron cyclotron and plasma frequencies. Panels (c)–(e) present the growth rate, frequency and wave number of the fastest-growing parallel and anti-parallel whistler waves at various values of core drift velocity u_c/v_A . The green bars in panels (c)–(e) indicate u_c/v_A values used in simulation runs presented in Section 3.

Acknowledgments

The work of I.K., I.V. and A.A. was supported by NASA grants 80NSSC21K0581 and 80NSSC23K0100. We would like to acknowledge high-performance computing support from Cheyenne (doi:10.5065/D6RX99HX) provided by NCAR's Computational and Information Systems Laboratory, sponsored by NSF grant No. 1502923. I.V. thanks the International Space Science Institute, Bern, Switzerland or supporting the working group on "Heliospheric Energy Budget: From Kinetic Scales to Global Solar Wind Dynamics".

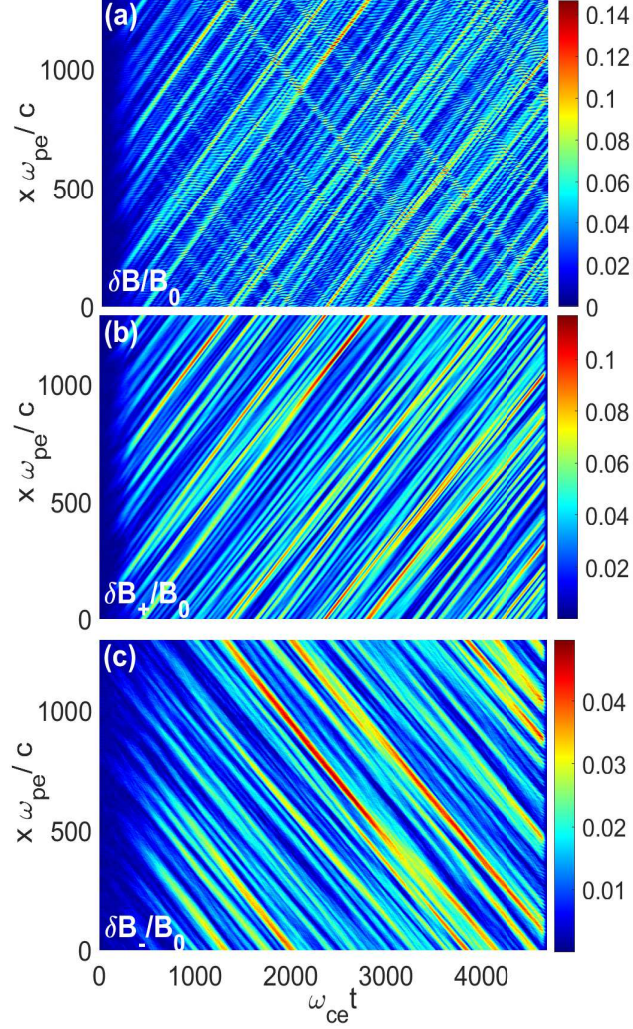


Figure 2: The results of a simulation run performed at $\beta_c = 1$, $A_h = 1.3$ and $u_c/v_A = -3$. Panel (a) presents the magnitude of magnetic field $\delta\mathbf{B}(x,t) = \delta B_y(x,t)\hat{y} + \delta B_z(x,t)\hat{z}$ perpendicular to background magnetic field $B_0\hat{x}$. Panels (b) and (c) demonstrate the magnitude of magnetic fields $\delta\mathbf{B}_+(x,t)$ and $\delta\mathbf{B}_-(x,t)$ corresponding to whistler waves propagating parallel and anti-parallel to the electron heat flux. The magnetic field fluctuations were decomposed into those propagating parallel and anti-parallel to the electron heat flux using the Fourier transform (Section 2).

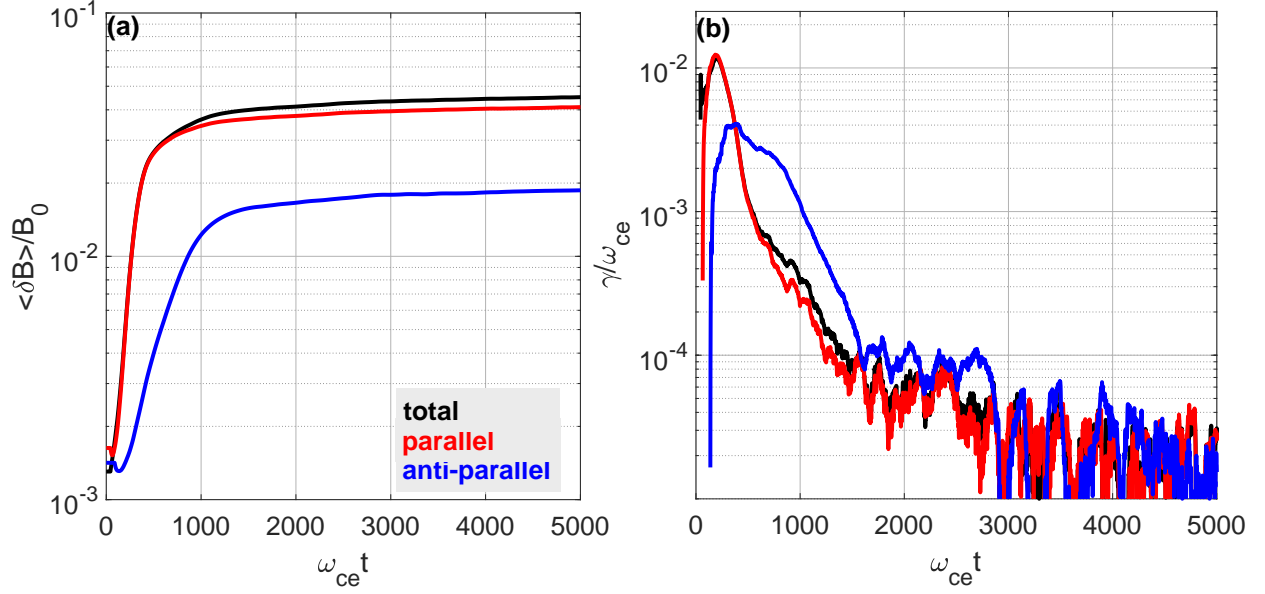


Figure 3: Panel (a) presents the temporal evolution of averaged magnetic field magnitudes of parallel and anti-parallel whistler waves observed in the simulation run shown in Figure 2; the magnetic field magnitudes were averaged over the simulation box, $\langle \delta B_{\pm} \rangle = \left[L^{-1} \int_0^L |\delta \mathbf{B}_{\pm}|^2 dx \right]^{1/2}$. Panel (b) presents the corresponding growth rates, $\gamma(t) = d/dt [\langle \delta B_{\pm} \rangle]$.

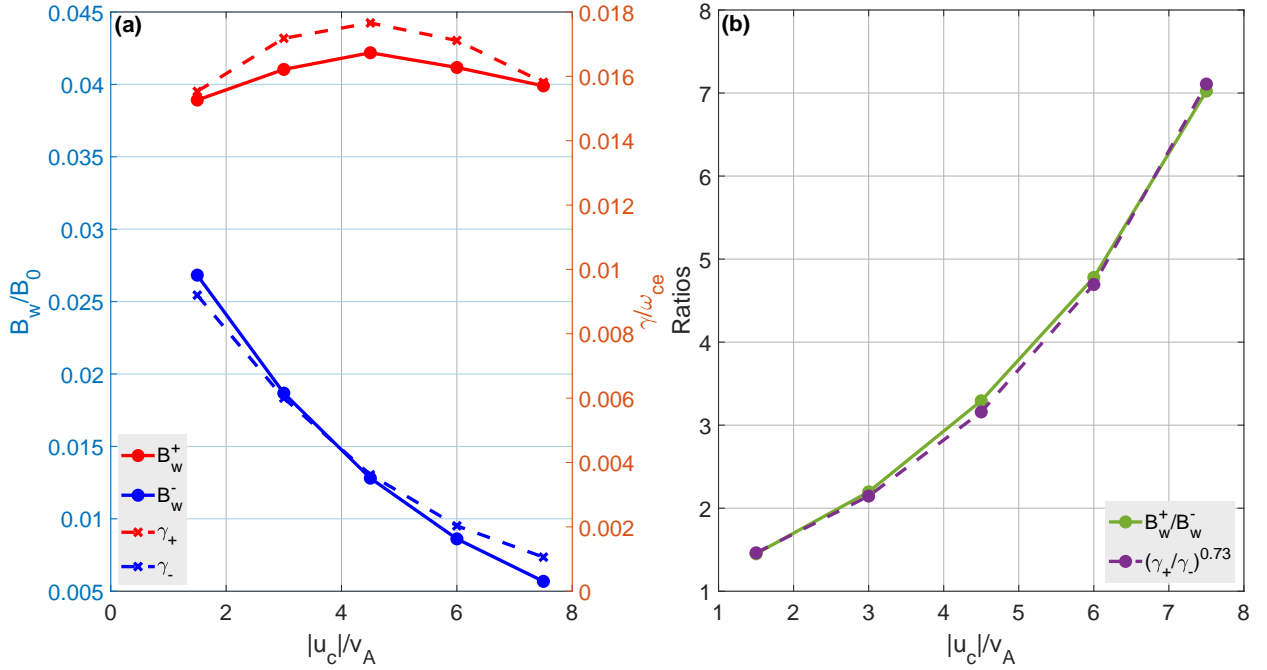


Figure 4: The results of simulation runs performed at $\beta_c = 1$ and $A_h = 1.3$, but various values of core electron drift velocity u_c / v_A (Section 3). Panel (a) presents saturated amplitudes B_w^+ / B_0 and B_w^- / B_0 of parallel and anti-parallel whistler waves along with their *initial* linear growth rates γ_+ / ω_{ce} and γ_- / ω_{ce} also shown in Figure 1. Panel (b) demonstrates that the ratios B_w^+ / B_w^- and γ_+ / γ_- are closely correlated, $B_w^+ / B_w^- \approx (\gamma_+ / \gamma_-)^{0.73}$.

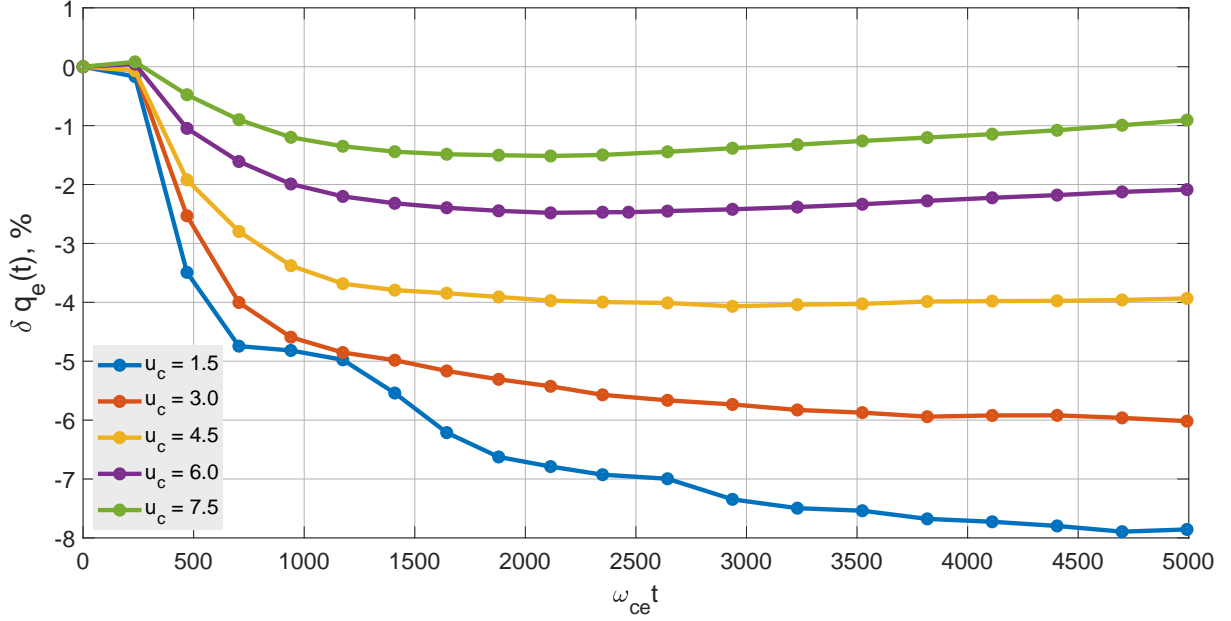


Figure 5: The temporal evolution of the electron heat flux in simulation runs performed at $\beta_c = 1$ and $A_h = 1.3$, but various values of core electron drift velocity u_c/v_A (Section 3). The panel presents the relative electron heat flux variation in percents, $\delta q_e = 100\% \cdot [q_e(t)/q_e(0) - 1]$, where $q_e(t)$ is the electron heat flux averaged over the simulation box.

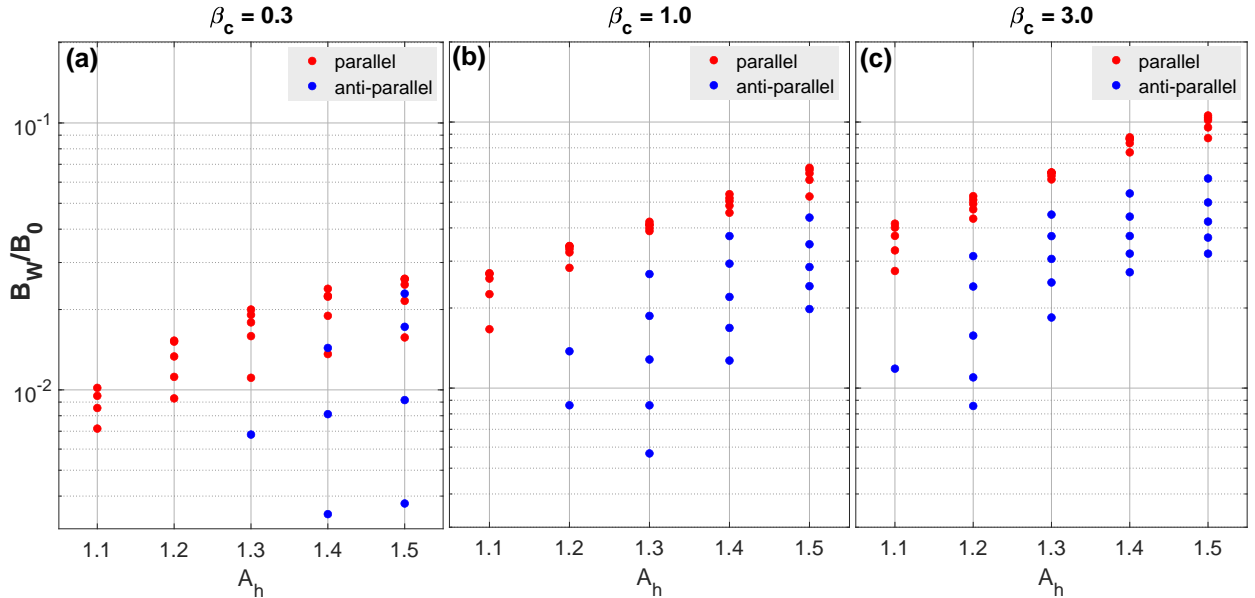


Figure 6: The results of all the 75 simulation runs performed at various values of core electron beta β_c , halo temperature anisotropy A_h and core electron drift velocity u_c/v_A (Table 1). Each of panels (a)–(c) presents saturated amplitudes of parallel and anti-parallel whistler waves observed in 25 simulation runs performed at $\beta_c = 0.3, 1$ and 3. Note that we present the amplitude of a whistler wave provided that its initial linear growth rate is larger than $10^{-3}\omega_{ce}$; otherwise the computation time of $5000\omega_{ce}^{-1}$ is insufficient for the whistler waves to saturate in our simulations.

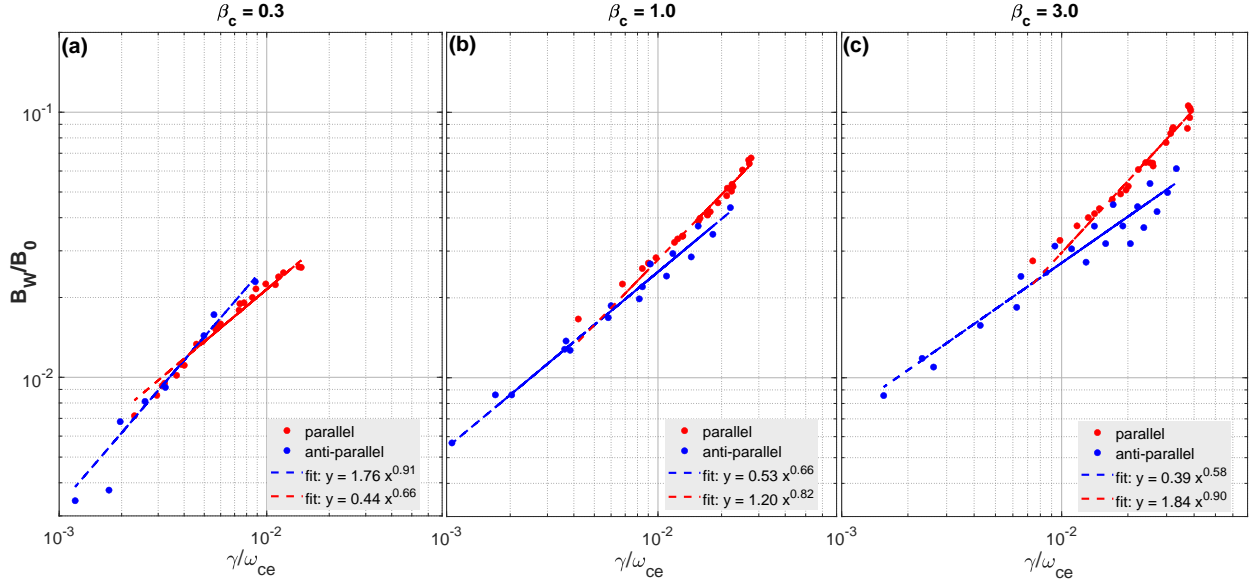


Figure 7: Each of panels (a)–(c) presents saturated amplitudes of parallel and anti-parallel whistler waves observed in 25 simulation runs performed at $\beta_c = 0.3, 1$ and 3 . The saturated amplitudes B_w/B_0 of the whistler waves are correlated with their initial linear growth rates γ/ω_{ce} and the best power law fits are indicated in the panels; the best fit parameters are also presented in Table 2.

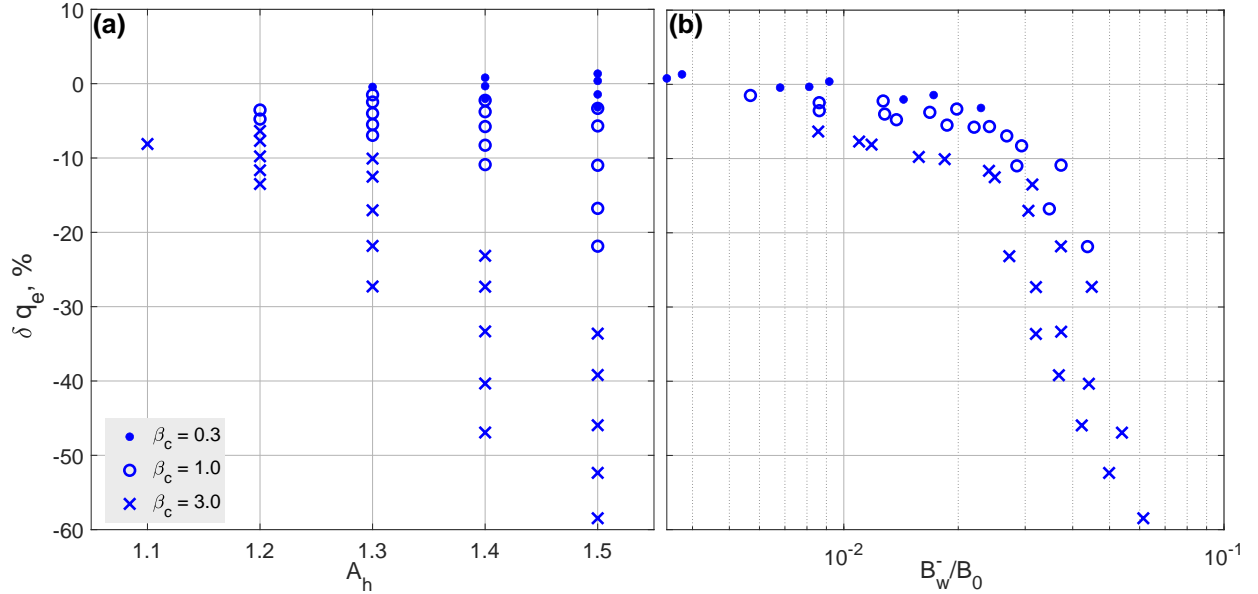


Figure 8: Panel (a) presents the relative electron heat flux variations reached by the end of our 75 simulation runs performed at various values of core electron beta β_c , halo temperature anisotropy A_h and core electron drift velocity u_c/v_A (Table 1). Panel (b) shows that the electron heat flux variation versus the saturated amplitude of whistler waves propagating anti-parallel to the electron heat flux (sunward whistler waves). Note that we only present results of those simulation runs, where sunward whistler waves had initial growth rates larger than $10^{-3}\omega_{ce}$ and could saturate over the computation time.

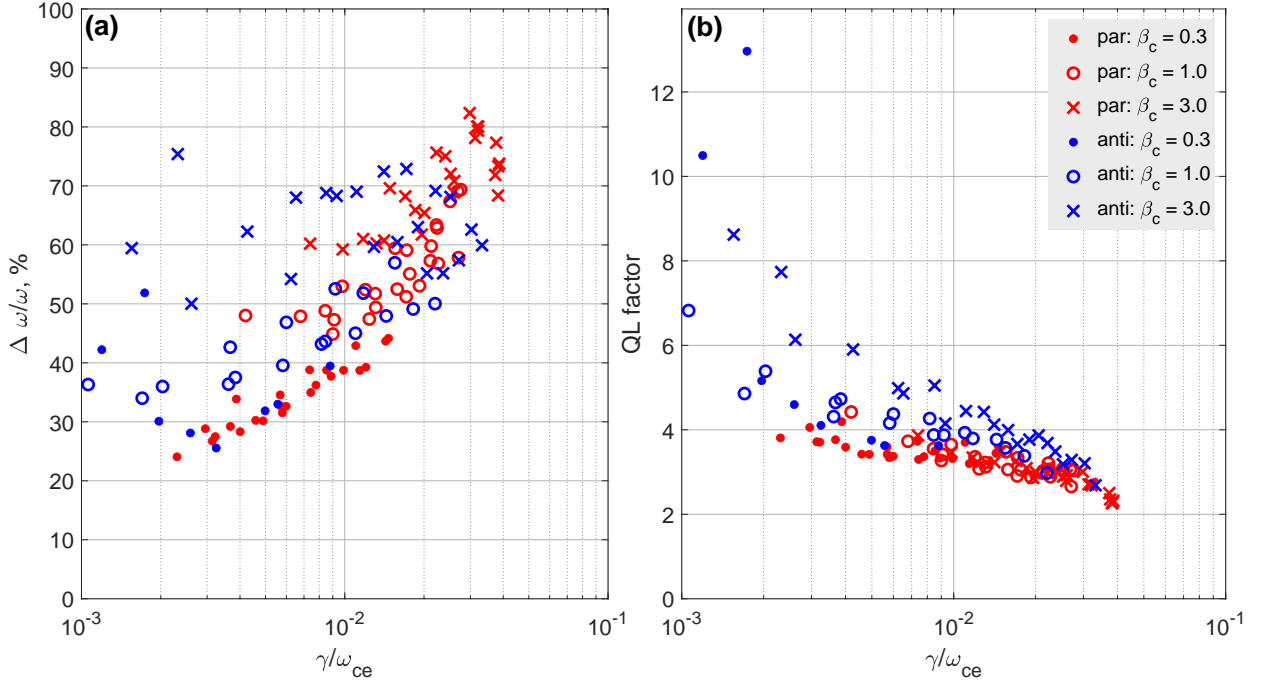


Figure 9: Panel (a) presents the relative spectral widths $\Delta\omega/\omega$ of parallel (anti-sunward) and anti-parallel (sunward) whistler waves observed over the saturation stage in the simulations performed at various background plasma parameters (Table 1). The spectral widths $\Delta\omega$ and central frequencies ω were computed using Gaussian fittings of the spectra. Panel (b) presents the ratio between the left- and right-sides of Eq. (3) computed separately for sunward and anti-sunward whistler waves and plotted versus their initial linear growth rates. The fact that this ratio is larger than one implies the nonlinear evolution and saturation of the whistler waves can be described within quasi-linear theory.

References

- [1] W. C. Feldman, J. R. Asbridge, S. J. Bame, M. D. Montgomery, and S. P. Gary. Solar wind electrons. *J. Geophys. Res.*, 80:4181–4196, November 1975.
- [2] W. G. Pilipp, K.-H. Muehlhaeuser, H. Miggenrieder, H. Rosenbauer, and R. Schwenn. Large-scale variations of thermal electron parameters in the solar wind between 0.3 and 1 AU. *J. Geophys. Res.*, 95:6305–6329, May 1990.
- [3] E. E. Scime, S. J. Bame, W. C. Feldman, S. P. Gary, J. L. Phillips, and A. Balogh. Regulation of the solar wind electron heat flux from 1 to 5 AU: ULYSSES observations. *J. Geophys. Res.*, 99:23, December 1994.
- [4] J. S. Halekas, P. L. Whittlesey, D. E. Larson, D. McGinnis, S. D. Bale, M. Berthomier, A. W. Case, B. D. G. Chandran, J. C. Kasper, K. G. Klein, K. E. Korreck, R. Livi, R. J. MacDowall, M. Maksimovic, D. M. Malaspina, L. Matteini, M. P. Pulupa, and M. L. Stevens. Electron heat flux in the near-Sun environment. *Astronomy & Astrophysics*, 650:A15, June 2021.
- [5] L. Spitzer and R. Härm. Transport Phenomena in a Completely Ionized Gas. *Physical Review*, 89:977–981, March 1953.
- [6] C. Salem, D. Hubert, C. Lacombe, S. D. Bale, A. Mangeney, D. E. Larson, and R. P. Lin. Electron properties and coulomb collisions in the solar wind at 1 au: Wind observations. *The Astrophysical Journal*, 585(2):1147, 2003.
- [7] S. D. Bale, M. Pulupa, C. Salem, C. H. K. Chen, and E. Quataert. Electron Heat Conduction in the Solar Wind: Transition from Spitzer-Härm to the Collisionless Limit. *Astrophys. J. Lett.*, 769:L22, June 2013.
- [8] S. P. Gary, R. M. Skoug, and W. Daughton. Electron heat flux constraints in the solar wind. *Physics of Plasmas*, 6:2607–2612, June 1999.
- [9] Y. Tong, S. D. Bale, C. Salem, and M. Pulupa. Observed instability constraints on electron heat flux in the solar wind. *arXiv e-prints*, January 2018.
- [10] Yuguang Tong, Ivan Y. Vasko, Anton V. Artemyev, Stuart D. Bale, and Forrest S. Mozer. Statistical Study of Whistler Waves in the Solar Wind at 1 au. *Astrophys. J.*, 878(1):41, June 2019.
- [11] Vamsee Krishna Jagarlamudi, Olga Alexandrova, Laura Berčič, Thierry Dudok de Wit, Vladimir Krasnoselskikh, Milan Maksimovic, and Štěpán Štverák. Whistler Waves and Electron Properties in the Inner Heliosphere: Helios Observations. *Astrophys. J.*, 897(2):118, July 2020.
- [12] C. Cattell, A. Breneman, J. Dombeck, E. Hanson, M. Johnson, J. Halekas, S. D. Bale, T. Dudok de Wit, K. Goetz, K. Goodrich, D. Malaspina, M. Pulupa, T. Case, J. C. Kasper, D. Larson, M. Stevens, and P. Whittlesey. Parker Solar Probe Evidence for the Absence of Whistlers Close to the Sun to Scatter Strahl and to Regulate Heat Flux. *Astrophys. J. Lett.*, 924(2):L33, January 2022.
- [13] W. C. Feldman, J. R. Asbridge, S. J. Bame, S. P. Gary, M. D. Montgomery, and S. M. Zink. Evidence for the regulation of solar wind heat flux at 1 AU. *J. Geophys. Res.*, 81:5207–5211, October 1976.
- [14] S. P. Gary and W. C. Feldman. Solar wind heat flux regulation by the whistler instability. *J. Geophys. Res.*, 82:1087–1094, March 1977.
- [15] C. Vocks, C. Salem, R. P. Lin, and G. Mann. Electron Halo and Strahl Formation in the Solar Wind by Resonant Interaction with Whistler Waves. *Astrophys. J.*, 627:540–549, July 2005.
- [16] Shinji Saito and S. Peter Gary. All whistlers are not created equally: Scattering of strahl electrons in the solar wind via particle-in-cell simulations. *Geophys. Res. Lett.*, 34(1):L01102, January 2007.
- [17] Stanislav Boldyrev and Konstantinos Horaites. Kinetic theory of the electron strahl in the solar wind. *Monthly Notices of the Royal Astronomical Society*, 489(3):3412–3419, November 2019.
- [18] Bofeng Tang, Gary P. Zank, and Vladimir I. Kolobov. Numerical Modeling of Suprathermal Electron Transport in the Solar Wind: Effects of Whistler Turbulence with a Full Diffusion Tensor. *Astrophys. J.*, 924(2):113, January 2022.
- [19] H. J. Beinroth and F. M. Neubauer. Properties of whistler mode waves between 0.3 and 1.0 AU from HELIOS observations. *J. Geophys. Res.*, 86:7755–7760, September 1981.
- [20] D. Lengyel-Frey, R. A. Hess, R. J. MacDowall, R. G. Stone, N. Lin, A. Balogh, and R. Forsyth. Ulysses observations of whistler waves at interplanetary shocks and in the solar wind. *J. Geophys. Res.*, 101(A12):27555–27564, December 1996.
- [21] C. H. K. Chen. Recent progress in astrophysical plasma turbulence from solar wind observations. *Journal of Plasma Physics*, 82(6):535820602, December 2016.

- [22] Y. Narita, R. Nakamura, W. Baumjohann, K. H. Glassmeier, U. Motschmann, B. Giles, W. Magnes, D. Fischer, R. B. Torbert, C. T. Russell, R. J. Strangeway, J. L. Burch, Y. Nariyuki, S. Saito, and S. P. Gary. On Electron-scale Whistler Turbulence in the Solar Wind. *Astrophys. J. Lett.*, 827(1):L8, August 2016.
- [23] S. P. Gary, W. C. Feldman, D. W. Forslund, and M. D. Montgomery. Heat flux instabilities in the solar wind. *J. Geophys. Res.*, 80:4197–4203, November 1975.
- [24] Daniel Verscharen, B. D. G. Chandran, E. Boella, J. Halekas, M. E. Innocenti, V. K. Jagarlamudi, A. Micera, V. Pierrard, Š. Štverák, I. Y. Vasko, M. Velli, and P. L. Whittlesey. Electron-Driven Instabilities in the Solar Wind. *Frontiers in Astronomy and Space Sciences*, 9:951628, August 2022.
- [25] M. Maksimovic, I. Zouganelis, J.-Y. Chaufray, K. Issautier, E. E. Scime, J. E. Littleton, E. Marsch, D. J. McComas, C. Salem, R. P. Lin, and H. Elliott. Radial evolution of the electron distribution functions in the fast solar wind between 0.3 and 1.5 AU. *Journal of Geophysical Research (Space Physics)*, 110:A09104, September 2005.
- [26] Š. Štverák, M. Maksimovic, P. M. Trávníček, E. Marsch, A. N. Fazakerley, and E. E. Scime. Radial evolution of nonthermal electron populations in the low-latitude solar wind: Helios, Cluster, and Ulysses Observations. *Journal of Geophysical Research (Space Physics)*, 114:A05104, May 2009.
- [27] J. S. Halekas, P. Whittlesey, D. E. Larson, D. McGinnis, M. Maksimovic, M. Berthomier, J. C. Kasper, A. W. Case, K. E. Korreck, M. L. Stevens, K. G. Klein, S. D. Bale, R. J. MacDowall, M. P. Pulupa, D. M. Malaspina, K. Goetz, and P. R. Harvey. Electrons in the Young Solar Wind: First Results from the Parker Solar Probe. *Astrophys. J. Supp.*, 246(2):22, February 2020.
- [28] Chadi S. Salem, Marc Pulupa, Stuart D. Bale, and Daniel Verscharen. Precision Electron Measurements in the Solar Wind at 1 au from NASA’s Wind Spacecraft. *arXiv e-prints*, page arXiv:2107.08125, July 2021.
- [29] I. Y. Vasko, V. Krasnoselskikh, Y. Tong, S. D. Bale, J. W. Bonnell, and F. S. Mozer. Whistler Fan Instability Driven by Strahl Electrons in the Solar Wind. *Astrophys. J. Lett.*, 871:L29, February 2019.
- [30] Daniel Verscharen, Benjamin D. G. Chandran, Seong-Yeop Jeong, Chadi S. Salem, Marc P. Pulupa, and Stuart D. Bale. Self-induced Scattering of Strahl Electrons in the Solar Wind. *Astrophys. J.*, 886(2):136, December 2019.
- [31] G. T. Roberg-Clark, O. Agapitov, J. F. Drake, and M. Swisdak. Scattering of Energetic Electrons by Heat-flux-driven Whistlers in Flares. *Astrophys. J.*, 887(2):190, December 2019.
- [32] A. Micera, A. N. Zhukov, R. A. López, M. E. Innocenti, M. Lazar, E. Boella, and G. Lapenta. Particle-in-cell Simulation of Whistler Heat-flux Instabilities in the Solar Wind: Heat-flux Regulation and Electron Halo Formation. *Astrophys. J. Lett.*, 903(1):L23, November 2020.
- [33] A. Micera, A. N. Zhukov, R. A. López, E. Boella, A. Tenerani, M. Velli, G. Lapenta, and M. E. Innocenti. On the Role of Solar Wind Expansion as a Source of Whistler Waves: Scattering of Suprathermal Electrons and Heat Flux Regulation in the Inner Heliosphere. *Astrophys. J.*, 919(1):42, September 2021.
- [34] Seong-Yeop Jeong, Joel B. Abraham, Daniel Verscharen, Laura Berčič, David Stansby, Georgios Nicolaou, Christopher J. Owen, Robert T. Wicks, Andrew N. Fazakerley, Jeffersson A. Agudelo Rueda, and Mayur Bakrania. The Stability of the Electron Strahl against the Oblique Fast-magnetosonic/Whistler Instability in the Inner Heliosphere. *Astrophys. J. Lett.*, 926(2):L26, February 2022.
- [35] Joel B. Abraham, Christopher J. Owen, Daniel Verscharen, Mayur Bakrania, David Stansby, Robert T. Wicks, Georgios Nicolaou, Phyllis L. Whittlesey, Jeffersson A. Agudelo Rueda, Seong-Yeop Jeong, and Laura Berčič. Radial Evolution of Thermal and Suprathermal Electron Populations in the Slow Solar Wind from 0.13 to 0.5 au: Parker Solar Probe Observations. *Astrophys. J.*, 931(2):118, June 2022.
- [36] Konstantinos Horaites and Stanislav Boldyrev. The heliospheric ambipolar potential inferred from sunward-propagating halo electrons. *Monthly Notices of the Royal Astronomical Society*, 515(4):5135–5144, October 2022.
- [37] C. Lacombe, O. Alexandrova, L. Matteini, O. Santolík, N. Cornilleau-Wehrlin, A. Mangeney, Y. de Conchy, and M. Maksimovic. Whistler Mode Waves and the Electron Heat Flux in the Solar Wind: Cluster Observations. *Astrophys. J.*, 796:5, November 2014.
- [38] D. Stansby, T. S. Horbury, C. H. K. Chen, and L. Matteini. Experimental Determination of Whistler Wave Dispersion Relation in the Solar Wind. *Astrophys. J. Lett.*, 829:L16, September 2016.
- [39] P. Kajdič, O. Alexandrova, M. Maksimovic, C. Lacombe, and A. N. Fazakerley. Suprathermal Electron Strahl Widths in the Presence of Narrow-band Whistler Waves in the Solar Wind. *Astrophys. J.*, 833:172, December 2016.

- [40] L. Berčič, D. Verscharen, C. J. Owen, L. Colombari, M. Kretzschmar, T. Chust, M. Maksimovic, D. O. Kataria, C. Anekallu, E. Behar, M. Berthomier, R. Bruno, V. Fortunato, C. W. Kelly, Y. V. Khotyaintsev, G. R. Lewis, S. Livi, P. Louarn, G. Mele, G. Nicolaou, G. Watson, and R. T. Wicks. Whistler instability driven by the sunward electron deficit in the solar wind. High-cadence Solar Orbiter observations. *Astronomy & Astrophysics*, 656:A31, December 2021.
- [41] M. Kretzschmar, T. Chust, V. Krasnoselskikh, D. Graham, L. Colombari, M. Maksimovic, Yu. V. Khotyaintsev, J. Soucek, K. Steinvall, O. Santolík, G. Jannet, J. Y. Brochot, O. Le Contel, A. Vecchio, X. Bonnin, S. D. Bale, C. Froment, A. Larosa, M. Bergerard-Timofeeva, P. Ferreau, E. Lorfèvre, D. Plettemeier, M. Steller, Š. Štverák, P. Trávníček, A. Vaivads, T. S. Horbury, H. O’Brien, V. Evans, V. Angelini, C. J. Owen, and P. Louarn. Whistler waves observed by Solar Orbiter/RPW between 0.5 AU and 1 AU. *Astronomy & Astrophysics*, 656:A24, December 2021.
- [42] A. Breneman, C. Cattell, S. Schreiner, K. Kersten, L. B. Wilson, III, P. Kellogg, K. Goetz, and L. K. Jian. Observations of large-amplitude, narrowband whistlers at stream interaction regions. *Journal of Geophysical Research (Space Physics)*, 115:A08104, August 2010.
- [43] C. Cattell, A. Breneman, J. Dombek, B. Short, J. Wygant, J. Halekas, Tony Case, J. C. Kasper, D. Larson, Mike Stevens, P. Whittesley, S. D. Bale, T. Dudok de Wit, K. Goodrich, R. MacDowall, M. Moncuquet, D. Malaspina, and M. Pulupa. Parker Solar Probe Evidence for Scattering of Electrons in the Young Solar Wind by Narrowband Whistler-mode Waves. *Astrophys. J. Lett.*, 911(2):L29, April 2021.
- [44] S. P. Gary, E. E. Scime, J. L. Phillips, and W. C. Feldman. The whistler heat flux instability: Threshold conditions in the solar wind. *J. Geophys. Res.*, 99:23, December 1994.
- [45] Y. Tong, I. Y. Vasko, M. Pulupa, F. S. Mozer, S. D. Bale, A. V. Artemyev, and V. Krasnoselskikh. Whistler Wave Generation by Halo Electrons in the Solar Wind. *Astrophys. J. Lett.*, 870:L6, January 2019.
- [46] Ilya V. Kuzichev, Ivan Y. Vasko, Angel Rualdo Soto-Chavez, Yuguang Tong, Anton V. Artemyev, Stuart D. Bale, and Anatoly Spitkovsky. Nonlinear Evolution of the Whistler Heat Flux Instability. *Astrophys. J.*, 882(2):81, Sep 2019.
- [47] S. P. Gary and H. Li. Whistler Heat Flux Instability at High Beta. *Astrophys. J.*, 529:1131–1135, February 2000.
- [48] I. Y. Vasko, I. V. Kuzichev, A. V. Artemyev, S. D. Bale, J. W. Bonnell, and F. S. Mozer. On quasi-parallel whistler waves in the solar wind. *Physics of Plasmas*, 27(8):082902, 2020.
- [49] V. Pierrard, M. Lazar, S. Poedts, Š. Štverák, M. Maksimovic, and P. M. Trávníček. The Electron Temperature and Anisotropy in the Solar Wind. Comparison of the Core and Halo Populations. *Solar Physics*, 291:2165–2179, August 2016.
- [50] III Wilson, Lynn B., Li-Jen Chen, Shan Wang, Steven J. Schwartz, Drew L. Turner, Michael L. Stevens, Justin C. Kasper, Adnane Osmane, Damiano Caprioli, Stuart D. Bale, Marc P. Pulupa, Chadi S. Salem, and Katherine A. Goodrich. Electron Energy Partition across Interplanetary Shocks. II. Statistics. *Astrophys. J. Supp.*, 245(2):24, December 2019.
- [51] III Wilson, Lynn B., Li-Jen Chen, Shan Wang, Steven J. Schwartz, Drew L. Turner, Michael L. Stevens, Justin C. Kasper, Adnane Osmane, Damiano Caprioli, Stuart D. Bale, Marc P. Pulupa, Chadi S. Salem, and Katherine A. Goodrich. Electron Energy Partition across Interplanetary Shocks. III. Analysis. *Astrophys. J.*, 893(1):22, April 2020.
- [52] O. V. Agapitov, T. Dudok de Wit, F. S. Mozer, J. W. Bonnell, J. F. Drake, D. Malaspina, V. Krasnoselskikh, S. Bale, P. L. Whittlesey, A. W. Case, C. Chaston, C. Froment, K. Goetz, K. A. Goodrich, P. R. Harvey, J. C. Kasper, K. E. Korreck, D. E. Larson, R. Livi, R. J. MacDowall, M. Pulupa, C. Revillet, M. Stevens, and J. R. Wygant. Sunward-propagating Whistler Waves Collocated with Localized Magnetic Field Holes in the Solar Wind: Parker Solar Probe Observations at 35.7 R_{\odot} Radii. *Astrophys. J. Lett.*, 891(1):L20, March 2020.
- [53] F. S. Mozer, O. V. Agapitov, S. D. Bale, J. W. Bonnell, T. A. Bowen, and I. Vasko. DC and Low-Frequency Electric Field Measurements on the Parker Solar Probe. *Journal of Geophysical Research (Space Physics)*, 125(9):e27980, September 2020.
- [54] A. Spitkovsky. Particle Acceleration in Relativistic Collisionless Shocks: Fermi Process at Last? *Astrophys. J. Lett.*, 682:L5, July 2008.
- [55] V. K. Jagarlamudi, T. Dudok de Wit, C. Froment, V. Krasnoselskikh, A. Larosa, L. Bercic, O. Agapitov, J. S. Halekas, M. Kretzschmar, D. Malaspina, M. Moncuquet, S. D. Bale, A. W. Case, J. C. Kasper, K. E. Korreck, D. E. Larson, M. Pulupa, M. L. Stevens, and P. Whittlesey. Whistler wave occurrence and the interaction with strahl electrons during the first encounter of Parker Solar Probe. *Astronomy & Astrophysics*, 650:A9, June 2021.

- [56] Ronald C. Davidson, David A. Hammer, Irving Haber, and Carl E. Wagner. Nonlinear Development of Electromagnetic Instabilities in Anisotropic Plasmas. *Physics of Fluids*, 15(2):317–333, February 1972.
- [57] V. I. Karpman. Nonlinear Effects in the ELF Waves Propagating along the Magnetic Field in the Magnetosphere. *Space Sci. Rev.*, 16(3):361–388, September 1974.
- [58] D. R. Shklyar. On the nature of particle energization via resonant wave-particle interaction in the inhomogeneous magnetospheric plasma. *Annales Geophysicae*, 29(6):1179–1188, June 2011.
- [59] R. Z. Sagdeev and A. A. Galeev. *Nonlinear Plasma Theory*. 1969.

This figure "Figure4.png" is available in "png" format from:

<http://arxiv.org/ps/2303.18214v1>